X-ray photoelectron spectroscopic study of impregnated $La_{0.4}Sr_{0.6}Ti_{0.8}Mn_{0.2}O_{3\pm d}$ anode material for high temperature-operating solid oxide fuel cell

Sung Hun Woo [a], Dae Soo Park [a], WonSeok Choi [b], Hyunil Kang [b], Seung-Wook Baek [c], Hyun-Suk Kim [d], Tae Ho Shin [e], Jun-Young Park [f], Harald Schlegl [g], Jung Hyun Kim [a,*]

[a] Department of Advanced Materials Science and Engineering, Hanbat National University, 125, Dongseo-Daero, Yuseong-Gu, Daejeon, 34158, Republic of Korea

[b] Department of Electrical Engineering, Hanbat National University, 125, Dongseo-Daero, Yuseong-Gu, Daejeon, 34158, Republic of Korea

[c] Center for Energy Materials Metrology, Division of Industrial Metrology, Korea Research Institute of Standards and Science (KRISS), 267, Gajeong-Ro, Yuseong-Gu, Daejeon, 34113, Republic of Korea

[d] Department of Materials Science and Engineering, Chungnam National University, 99, Daehak-Ro, Yuseong-Gu, Daejeon, 34134, Republic of Korea

[e] Energy and Environment Division, Korea Institute of Ceramic Engineering and Technology (KICET), 101, Soho-Ro, Jinju-Si, Gyeongsangnam-Do 52851, Republic of Korea

[f] HMC, Department of Nanotechnology and Advanced Materials Engineering, Sejong University, 209, Neungdong-Ro, Gwangjin-Gu, Seoul, 05006, Republic of Korea

[g] Engineering Department, Lancaster University, Bailrigg, Lancaster LA1 4YW, United Kingdom

Corresponding author:*

Jung Hyun Kim: jhkim2011@hanbat.ac.kr, jhkim1870@gmail.com, Tel: +82-42-821-1239, Fax: +82-42-821-1592, Department of Advanced Materials Science and Engineering, Hanbat National University, 125, Dongseo-Daero, Yuseong-Gu, Daejeon, 34158, Republic of Korea

Abstract

In this study, the chemical states of a powder type and an impregnated type of the $La_{0.4}Sr_{0.6}Ti_{0.8}Mn_{0.2}O_{3\pm d}$ (LSTM) oxide system were investigated along with its electrical conductivities in order to apply these materials as alternative anode materials for high temperature-operating Solid Oxide Fuel Cells (HT-SOFCs).

The Ni / 8YSZ samples with LSTM impregnated into the pores created by partially removing nickel, Ni / 8YSZ (Ni (R) / 8YSZ), showed much higher electrical conductivity values than those of unimpregnated Ni / 8YSZ (Ni (E) / 8YSZ) samples under dry H_2 fuel condition.

Reduction of Mn^{4+} to Mn^{3+} was observed when LSTM was reduced. Additional reduction properties of Mn^{2+} from Mn^{3+} and satellite peaks were found when impregnated LSTM was coated onto a Ni / 8YSZ substrate. The reduction of the charge state of Ti contained in LSTM showed the same behavior as the reduction property of Mn. However, a satellite peak identified as metal Ti was only observed when impregnated LSTM was coated on a selectively Ni-removed Ni / 8YSZ (Ni (R) / 8YSZ) substrate.

Keywords: High temperature-operating solid oxide fuel cell (HT-SOFC); Anode; Electrical conductivity; X-ray photoelectron spectroscopy (XPS); Binding energy (BE); Impregnation

1. Introduction

Alternative anode materials for Solid Oxide Fuel Cells (SOFCs) fabricated with various strategies such as using modified Ni-YSZ cermet [1-4], using a noble metal [5-8] or synthesizing a new single phase perovskite oxide [9,10] have been focused on because of the deterioration of the SOFC performance caused by carbon deposition. In the case of the carbon formation, we observed that significant dimensional changes of the Ni-YSZ cermet via carbon dissolution upon exposure to dry methane occurred and carbon formation led to the deactivation of the SOFC anode via three-dimensional expansion of the material [11].

Among the various perovskite based oxide systems, titanates have been extensively investigated as an anode material for SOFCs because of their stability, electro-catalytic activity as well as their electrical characteristics caused by Ti^{3+} and Ti^{4+} [12]. When the titanate type complex perovskite $La_{0.2}Sr_{0.8}TiO_3$ was applied as an anode barrier in a tubular SOFC, it showed stable electrochemical properties under biogas comprised of 63 % CH_4, 34% CO_2 and 3% H_2O for 12 days without carbon deposition [13]. $La_4Sr_8Ti_{11}Mn_{0.5}Ga_{0.5}O_{37.5}$ synthesized by partly substituting titanium by Mn and Ga showed excellent maximum power density and lower polarization without detected carbon residues working from 850 ^oC to 950 ^oC for 2 days [14, 15].

The titanium doped ferrite perovskite, $La_{0.7}Sr_{0.3}Fe_{0.7}Ti_{0.3}O_3$ (LSFT) was used for anode materials in a single cell comprised of LSFT / $Sm_{0.2}Ce_{0.8}O_2$ (SDC: barrier layer)/ 8 mol% yttria stabilized zirconia (8YSZ:electrolyte) / $(La_{0.75}Sr_{0.25})_{0.95}MnO_3$ (LSM-YSZ:composite cathode) at 850 ^oC, this single cell did not show performance degradation and voltage fluctuation under the constant current density of 200 mA cm^{-2} for 1 day at 850^oC, using CH_4 containing 3% H_2O as a fuel supplied at the LSFT anode side because of the enhanced stability of this anode and its electro-catalytic properties [16].

Our group recently synthesized an $La_{0.4}Sr_{0.6}Ti_{0.8}Mn_{0.2}O_{3\pm d}$ (LSTM) oxide system and

analyzed the electrochemical properties of LSTM in a composite anode fabricated using an impregnation technique on a porous 8YSZ scaffold structure [17]. In the results of this study, the impregnated LSTM was found to generate a continuously connected oxide layer covering the porous structure under oxidizing conditions. The structure of this cover layer changed to very small fine particles under reducing condition, which resulted in an enhanced triple phase boundary (TPB). Significantly, the changed microstructure played a role in increasing the conductivity of the reduced composite by two orders of magnitude comparing to the conductivity of the anode under oxidizing conditions.

In a related research study [18], we also reported on the catalytic effect of the impregnated LSTM oxide system as a potential composite anode material with CeO_2 and Pd in high temperature SOFCs; the application of CeO_2 reduced both the ohmic resistance and the polarization resistance of a single cell fabricated via the tape casting process. The power density of a cell with an anode containing 20 wt% of CeO_2, 30 wt% of YSZ and 50 wt% of LSTM was increased compared to a cell with an anode of LSTM impregnated into a porous 8YSZ scaffold.

In this study, based on the microstructure, electrical conductivity and electrochemical characteristics of the previously reported LSTM [17, 18], we have conducted electrical conductivity studies of two additional composite anode substrates. LSTM was impregnated into the scaffold structure of Ni / 8YSZ (Ni (E) / 8YSZ) and into a scaffold structure of Ni / 8YSZ with Ni partially removed (Ni (R) / 8YSZ). X-ray Photoelectron Spectroscopy (XPS) analysis was used to investigate the chemical state of the non-impregnated powder type and the LSTM oxide impregnated type under various experimental conditions. Heat treatment under oxidizing and reducing atmosphere was applied to stimulate working condition as alternative anode materials for high temperature-operating SOFCs (HT-SOFCs). Especially, the effect of Ni contacting LSTM on the charge states of transition metals contained in LSTM,

such as Mn and Ti, were analyzed to explore application of composites as an anode material for HT-SOFCs.

2. Experimental

2.1. Sample preparation and phase synthesis

The $La_{0.4}Sr_{0.6}Ti_{0.8}Mn_{0.2}O_{3\pm d}$ (LSTM) oxide system was synthesized using the glycine nitrate process (GNP) technique because GNP can not only rapidly synthesize the perovskite oxide system comprised of various types of elements but also be used to obtain very fine powders [19, 20]. Detailed experimental procedures for this synthesis can be found elsewhere [17, 18, 21].

As raw materials for the synthesis of LSTM oxide system, the solution for the GNP process of LSTM was prepared with Lanthanum nitrate ($La(NO_3)_3$-$6H_2O$), Strontium nitrate ($Sr(NO_3)_2$), Dihydroxy-bis (ammonium lactato)-titanium (IV) ($[CH_3CH(O^-)CO_2$-$NH_4]_2$-$Ti(OH)_2$) and Manganese nitrate ($Mn(NO_3)_2$-$4H_2O$). The weighed salts and added glycine were dissolved in de-ionized water in a molar relationship of 2:1, in amounts providing a metal ion ratio of La:Sr:Ti:Mn=0.4:0.6:0.8:0.2.

The aqueous solution was heated from room temperature to 300 ^oC until it was dehydrated. The dried LSTM powder was pressed into pellets using a square type metal mold with a size of 10 cm by 10 cm; materials were then calcined in air condition at 1200 ^oC for 4 h to convert the dried oxides into the desired perovskite phase. After finishing the calcination process of LSTM, the pelletized powders were grinded and using a wet ball-milling process with acetone and zirconia balls for 24h.

X-ray diffraction (XRD) patterns of the prepared samples were obtained in a Philips diffractometer using Cu radiation (λ= 0.15418 nm). The obtained data were matched with

reference data for identification of the crystal structures.

2.2. Fabrication of NiO / 8YSZ substrate and Selectively Ni-removed NiO / 8YSZ substrate

NiO powder (J.T. Baker, USA) and 8 mol% yttria stabilized zirconia (8YSZ, Tosho, Japan) powder were mixed at a weight ratio of 6:4 for the fabrication of the NiO / 8YSZ substrate. In addition, 15 wt% of carbon black (J.T. Baker, USA) used as the pore former and 1wt% of Butvar B-98 (Sigma) as a binder were added to the mixture of NiO / 8YSZ.

The mixtures for the fabrication of the substrate were ball-milled for 24 h using ethanol as medium. The powders dried in the oven were pulverized using an agate mortar and sieved to a size of 100 micro mesh. The mixed powders were pressed into pellets and then sintered at 1450 ^{o}C for 2 h. The abbreviation Ni (E) / 8 YSZ was used for the NiO / 8YSZ substrate obtained by this method.

For the partial removal of Ni from the NiO / 8YSZ substrate it had to be reduced to Ni / 8YSZ because metallic Ni can be easily removed through leaching with an HNO_3 based solution; in the fabricated Ni/YSZ composite this can result in an increase in the porosity beyond the porous structure that existed previously. The pores are generally caused by the pore former, but the nickel leaching in the Ni/YSZ composite generates additional porosity from Ni removal. For this reason, fabricated NiO / 8YSZ substrates were exposed to reducing condition by supplying 3.9 % H_2 / Ar balance gas at 930 ^{o}C for 20 h in order to reduce the NiO in the substrate to Ni.

These substrates were dipped into an acid based solution consisting of a 1:1 volume ratio of HNO_3-H_2O for 5 minutes. After the dipping process into the HNO_3-H_2O solutions, these substrates were thoroughly washed with deionized water to remove any excess HNO_3. After

the washing process of the Ni / 8YSZ substrates they were dried in an oven at 80 °C. The partially Ni removed Ni / 8YSZ substrate in this way was also initialized as Ni (R) / 8YSZ.

2.3. Impregnation process and prepared samples

To impregnate the LSTM solution into the NiO / 8YSZ substrate and into the selectively Ni removed porous structure, LSTM precursor solutions were utilized with the same LSTM solution process specified in Experimental section 2.1., but without addition of glycine. Glycine was abandoned to avoid swelling problems caused by the repeated impregnation process. Using a syringe, the solutions were slowly dropped onto the surfaces of the two porous substrates, i.e. the NiO / 8YSZ substrate and the selectively Ni removed porous structure. When the structures became saturated with solution, the samples were heated to 500 °C in air to evaporate the solvent. This process was repeated many times until the desired weight of 3wt% LSTM precursor on top of the original weight of the NiO/8YSZ or Ni(R)/8YSZ substrate was reached. The cells were then finally calcined at 1200 °C for 4 h in air.

2.4. Preparation of samples for XPS and Electrical conductivity

For the investigation of LSTM under oxidizing and reducing conditions, and as a substance on its own versus a substance in contact with Ni/YSZ after impregnation into a cermet, four different LSTM samples were fabricated. LSTM-(1) and LSTM-(2) are oxidized and reduced specimens of LSTM powder. LSTM-(3) is LSTM impregnated into a NiO/YSZ cermet, which is subsequently reduced. LSTM-(4) is LSTM impregnated into a different Ni/YSZ cermet, a cermet with parts of the Ni removed before the impregnation of LSTM and subsequently reduced. Detailed specification about the fabrication of all these four LSTM samples for XPS analysis is provided in Table 1.

For the XPS analysis, a VG-Scientific ESCALAB 250 spectrometer (UK) with a monochromatic X-ray source was used. Detailed experimental procedures for this synthesis can be found elsewhere [21-24].

Table 1. Summary of LSTM samples with respect to various experimental conditions

Initial of samples	**Experimental conditions**
LSTM-(1)	1. The prepared solution for the GNP process of using Lanthanum nitrate ($La(NO_3)_3$-$6H_2O$), Strontium nitrate ($Sr(NO_3)_2$), Dihydroxy-bis (ammonium lactato)-titanium (IV) ($[CH_3CH(O^-)CO_2$-$NH_4]_2$-$Ti(OH)_2$) and Manganese nitrate ($Mn(NO_3)_2$-$4H_2O$). 2. Heat treatment from room temperature to 300 ^oC until the prepared solution was dehydrated. 3. Calcination in air condition at 1200 ^oC for 4 h.
LSTM-(2)	1. LSTM-(1) exposed to the reducing condition by supplying 99.9% H_2 at 900^oC for 4 h.
LSTM-(3)	1. Preparation of NiO / 8YSZ substrates. The fabrication processes to prepare the NiO / 8YSZ substrates were explained in the first and second paragraphs of section 2.2. 2. Impregnation of the 3 wt% LSTM solution into a NiO / 8YSZ (Ni (E) / 8 YSZ) substrate. 3. Heat treatment at 1200 ^oC for 4h in air condition and then cooling to room temperature in air condition. 4. After finishing the process 3, heat treatment at 900 ^oC for 4h at reducing atmosphere using 99.9% H_2 and then cooling to room temperature continuously supplying H_2.
LSTM-(4)	1. Preparation of Ni / 8YSZ substrates. The fabrication processes to prepare the Ni / 8YSZ substrates were explained in the third and fourth paragraphs of section 2.2. 2. Impregnation of the 3 wt% LSTM solution into a partially Ni-removed

	Ni / 8YSZ (Ni (R) /8YSZ). 3. Heat treatment at 1200 °C for 4h in air condition and then cooling to room temperature in air condition. 4. After finishing the process 3, heat treatment at 900 °C for 4h at reducing atmosphere using 99.9% H_2 and then cooling to room temperature continuously supplying H_2.

Electrical conductivity measurements were conducted using a four-terminal DC arrangement in a custom jig with a Keithley 2400 Source Meter over a temperature range from 50°C to 900°C at a rate of 5 °C/min in dry and humidified H_2 /Ar gas mix (3.9 % H_2 / Ar balance gas).

3. Results and discussion

3.1. XRD measurement of LSTM

Fig. 1 shows the XRD patterns of $La_{0.4}Sr_{0.6}Ti_{0.8}Mn_{0.2}O_{3\pm d}$ (LSTM) under various atmospheric conditions. LSTM calcined at 1200°C for 4 h in air was used as the oxidized sample and well as a base material for subsequent reductions carried out under dry and wet H_2 at 930 °C.

The peaks measured in the vicinity of 2θ=34.9 and 40.5° indicate the existence of the undesired oxide phase MnO (JCPDS PDF 01-075-6876), the peaks of this phase show only in the spectra of the reduced samples. The existence of another undesired oxide phase Mn_2O_3 (JCPDS PDF 01-076-7064) was indicated by peaks found in the vicinity of 2θ=38.0° showing in all the spectra, under air condition as well as in both reduced samples.

The XRD spectra in Fig. 1 summarize all the peaks of the undesired oxide phases and, in addition, the indexed primary peaks of LSTM.

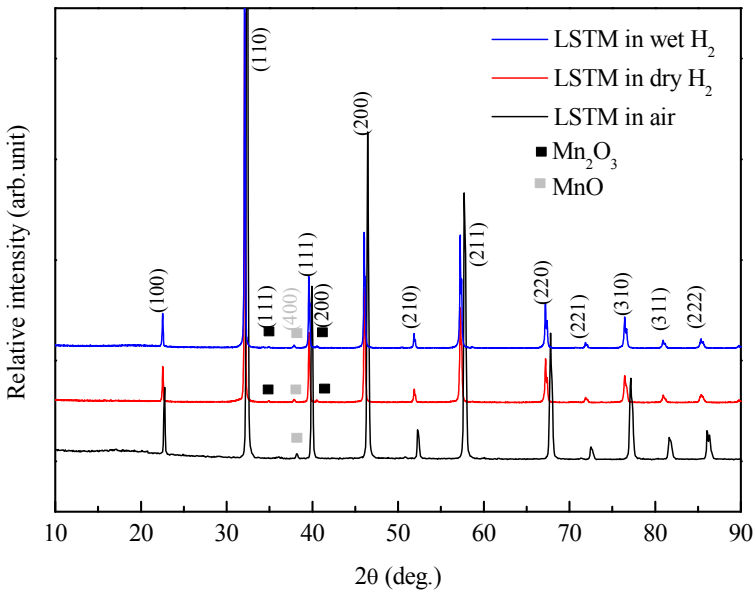

Fig. 1 XRD results of LSTM under various experimental conditions such as in dry-wet H_2 and in air condition at 930 °C.

Fig. 2 shows the XRD results to confirm the absence of reactivity between the phases of LSTM, Ni, NiO and 8YSZ at fabrication temperature. Reactivity tests were carried out by mixing the anode materials (Ni, NiO and 8YSZ) and LSTM in a 1: 1 mass ratio. These mixtures were heat-treated at 1200 °C for 2 h in air. The mixture of LSTM and NiO was exposed to the H_2 condition at the same temperature as explained above.

From XRD patterns shown as Fig. 2, no peaks related to any new secondary phases were observed for these mixtures. It can be clearly identified that these four materials remain in their unique phases without any kinds of reaction. Therefore, the XRD results shown as Fig. 2 proved that there are no chemical reactions between LSTM, NiO (or Ni) and 8YSZ at 1200 °C under air and H_2 condition. No performance degradation caused by the emergence of secondary phases can be expected when applying these materials to a single cell of a solid oxide fuel cell.

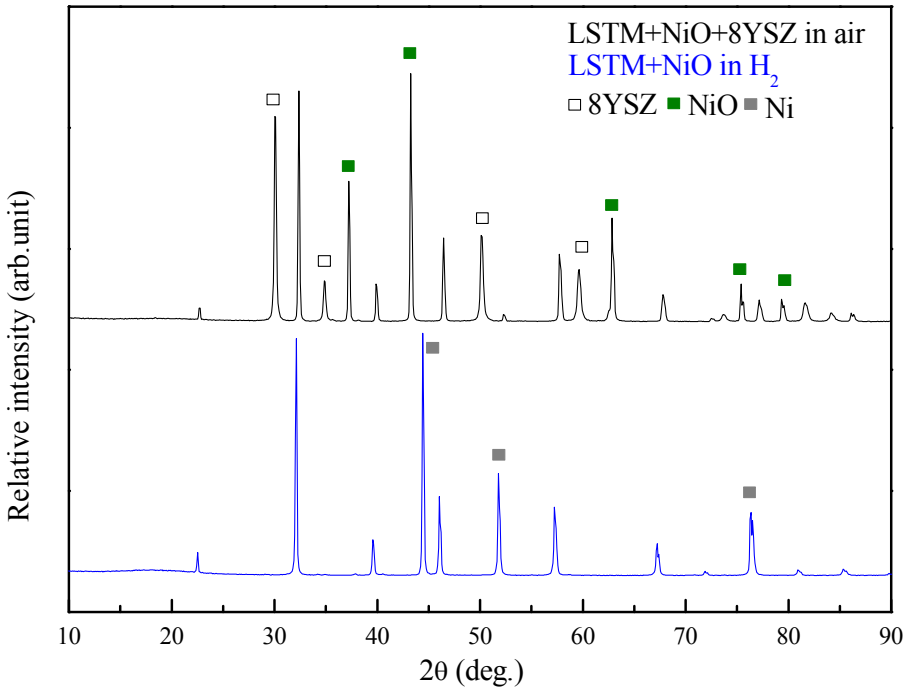

Fig. 2 XRD results of a mixture of LSTM, NiO and 8YSZ at 1200°C for 2 h under air and H_2 condition.

3.2. Electrical conductivity of LSTM

Fig. 3 shows the electrical conductivity properties of LSTM impregnated samples of a selectively Ni removed Ni (R) / 8YSZ substrate. It is worth considering that this substrate has a relatively more porous structure than Ni (E) / 8YSZ.

Considering the conductivity composite samples of LSTM impregnated into Ni (R) / 8YSZ substrates, the electrical conductivity values of samples impregnated with LSTM were surprisingly much higher than those of the pure Ni (E) / 8YSZ sample without LSTM, both measured under dry H_2 reducing conditions. For example, an LSTM impregnated sample shows the electrical conductivity values of 2041.2, 1877.4, 1764.3 S/cm at 700, 800 and 900 °C respectively under dry H_2. Observing the conductivity tendency of impregnated LSTM into

Ni free Ni (R) / 8YSZ substrate, it also shows the metallic behavior found in Ni (E) / 8YSZ. The magnitude of the electrical conductivity values observed in LSTM on Ni (R) / 8YSZ is also much higher than that of the unimpregnated Ni (E) / 8YSZ under dry H_2 condition. These characteristics are the same in wet reducing conditions. In addition, it can be seen that all conductivity values measured under dry H_2 conditions are higher than those measured under wet H_2 conditions.

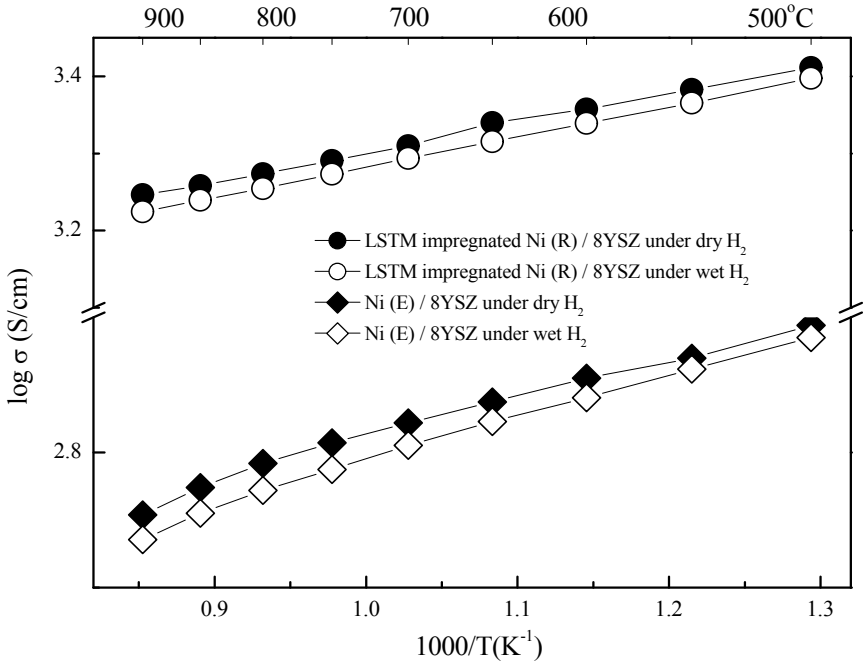

Fig. 3 Summary of the electrical conductivities of LSTM impregnated Ni (R) / 8YSZ and pure Ni (E) / 8YSZ under dry and wet H_2 condition from 500 to 900 °C.

3.3. Wide scan results

Fig. 4 shows the wide scan X-ray photoelectron spectroscopy (XPS) results for the LSTM oxide system carried out under various experimental conditions with respect to the binding energy (BE) ranges.

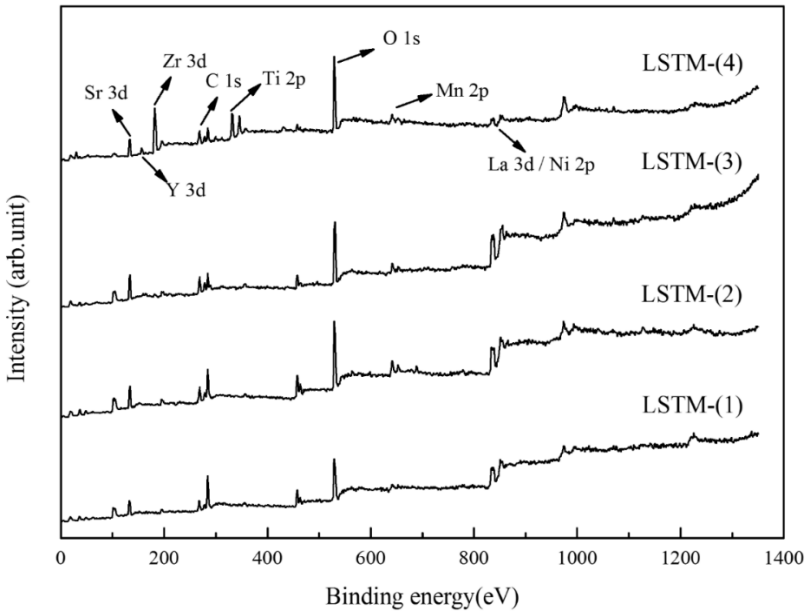

Fig. 4 Wide scan spectra of $La_{0.4}Sr_{0.6}Ti_{0.8}Mn_{0.2}O_{3\pm d}$ (LSTM) oxide system.

The existence of La, Sr, Ti and O as the atoms present in LSTM, and also of elemental C was observed in the wide scan results were observed; each element is ascribed to its corresponding BE range [25]. In addition, the spectra of the Zr, Y and Ni comprising the Ni (E) / 8YSZ and Ni (R) / 8YSZ substrate were also measured in LSTM-(3) and LSTM-(4) samples; these spectra originated from the vicinity of the corresponding BE ranges as well; this is because LSTM was impregnated onto Ni (E) / 8YSZ and Ni (R) / 8YSZ substrate. The carbon peak measured at around 284.4 eV was utilized for standard reference for the XPS calibration [26].

3.4. XPS spectra of O 1s

The O 1s spectra of LSTM-(1), (2), (3) and (4) with different conditions of LSTM are shown in Fig. 5. One merged peak shown in Fig. 5 was deconvoluted into a lower binding energy (LBE) and higher binding energy (HBE) due to binding energy differences because the LBE is ascribed to oxygen in the lattice and the HBE to adsorbed oxygen-containing species near the

surfaces [24].

The peak shifts with respect to the binding energy and the calculated area % from the deconvoluted peaks are summarized in Table 2. The BEs of the oxygen spectra caused by LBE are located at similar ranges in LSTM-(1), (2) and (4) but not in the LSTM-(3) sample. When LSTM was exposed to a reducing environment, however, the HBE peaks of the reduced LSTM shifted to lower energy ranges, although the BEs of each oxygen group were shown to have similar values.

In the results calculated for the LSTM-(1) and (2) samples, the values of area % occupied by LBE are 47.03 % and 50.28 %, respectively; these values show a 3.25 % increase in LBE when LSTM was heat-treated under a reducing environment. The increased area % of LSTM-(2) is due to the fact that oxygen ions were incorporated into the lattice of LSTM resulting in a larger amount of oxygen ions attached under reducing conditions. Therefore, it can be predicted that the movement of oxygen ions through the lattice will be slower under reducing conditions. In the XPS investigation of LSTM-(3) and (4), the samples behaved as expected considering the presence / absence of a preceding Ni removal step at the anode; the areas occupied by LBE are 32.93 % and 42.69 %, respectively, both these values are smaller than that of LSTM-(2). This implies that LSTM-(3) and (4) contained higher oxygen vacancy portions than LSTM-(2) and as a result, an enhanced oxygen ion penetration path. Therefore, the decrease of the area % occupied by LBE can be interpreted as an increase in the concentration of the oxygen vacancies and also an increase of the mobility of the oxygen ions in the LSTM-(3) and LSTM-(4) samples compared to those in the LSTM-(2) sample.

The obtained XPS results for the O 1s orbitals of the samples LSTM-(2), LSTM-(3) and LSTM-(4) seem to suggest an influence of the surface contact of metallic nickel to LSTM under reducing conditions. The direct contact with metallic nickel constitutes a pull factor for oxygen

ions to migrate from their lattice positions to the surface of LSTM grains, thus depleting the perovskite lattice of oxygen ions and creating additional oxygen vacancies within this lattice. This effect is strongest in LSTM-(3) for the simple reason that the nickel content is highest in this sample, the effect is weaker but still observable in LSTM-(4), where the nickel content is lower due to precedent part removal of nickel by HNO_3 leaching.

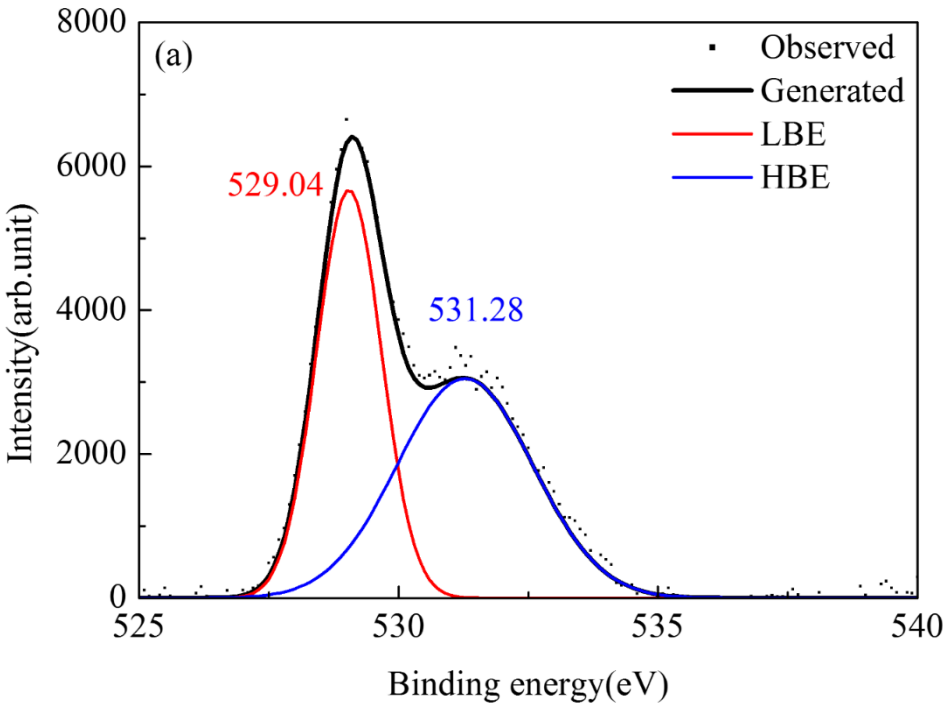

Fig. 5 (a)

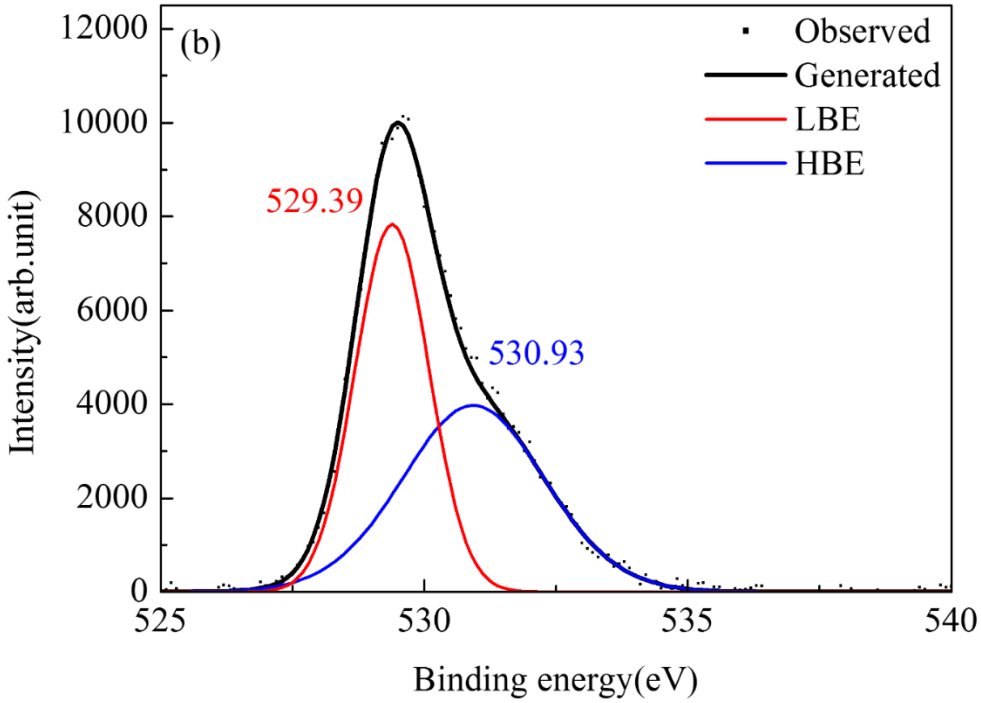
(b)
Observed
Generated
LBE
HBE
529.39
530.93
Intensity(arb.unit)
Binding energy(eV)
12000
10000
8000
6000
4000
2000
0
525
530
535
540

Fig. 5 (b)

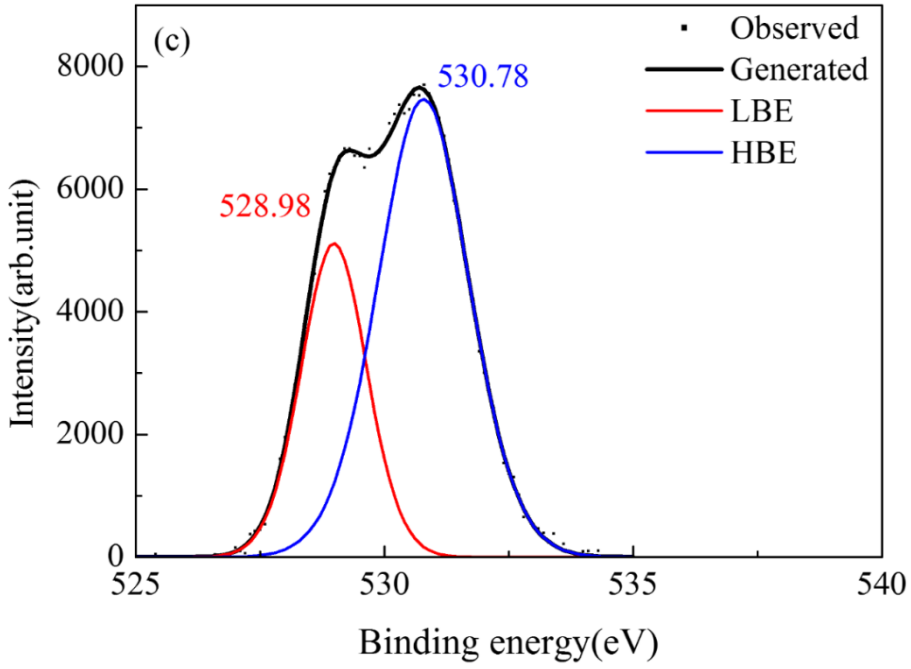
(c)
Observed
Generated
LBE
HBE
530.78
528.98
Intensity(arb.unit)
Binding energy(eV)
8000
6000
4000
2000
0
525
530
535
540

Fig. 5 (c)

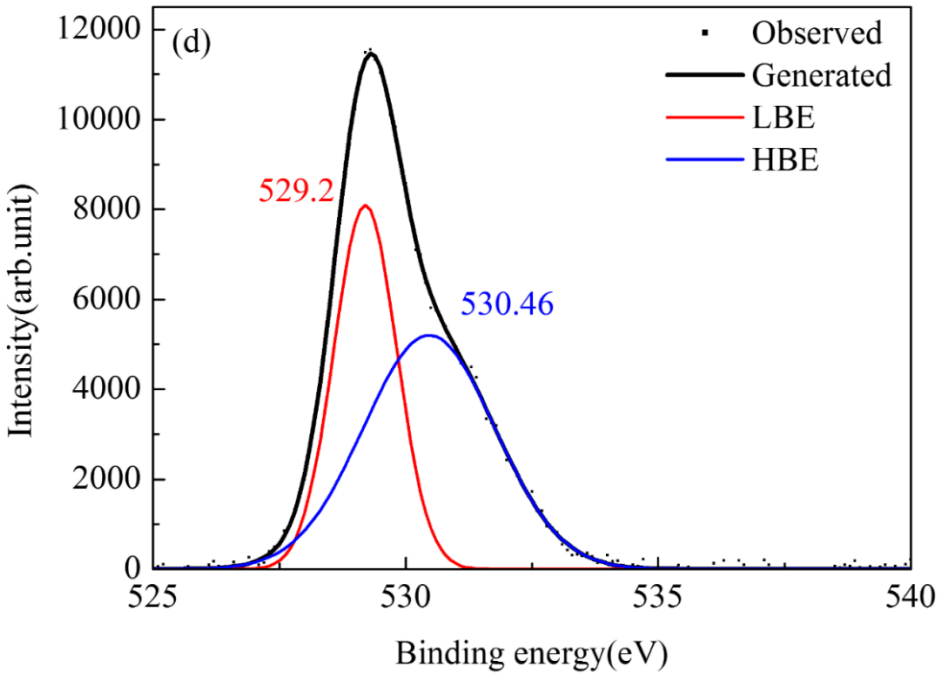

Fig. 5 (d)

Fig. 5 Measured Oxygen 1s peaks and deconvolution peaks of LSTM (a) LSTM-(1), (b) LSTM-(2), (c) LSTM-(3) and (d) LSTM-(4).

Table 2. Binding energy (BE) and % area of the oxygen peaks

	BE peak shift		**% Area**	
	LBE (eV)	**HBE (eV)**	**LBE**	**HBE**
LSTM-(1)	529.04	531.28	47.03	52.97
LSTM-(2)	529.39	530.93	50.28	49.72
LSTM-(3)	528.98	530.78	32.93	67.07
LSTM-(4)	529.20	530.46	42.69	57.31

3.5. XPS spectra of Mn

Fig. 6 show the XPS spectra of Mn in the LSTM oxide system. From these measured XPS results, the spin orbital splitting has resulted in two separated main peaks with having relatively lower binding energy ranges and higher binding energy ranges; the peaks found in the lower binding energy are ascribed to $2p_{3/2}$ of Mn 2p and the peaks measured at the higher binding energy originate from $2p_{1/2}$ of Mn 2p.

The charge state of Mn can be generally said to be comprised of +2, +3 and +4 charges and, therefore, when considering the stable oxides with respect to the charge state, each +2, +3 and +4 charge state can be said to originate from the oxide forms of MnO, Mn_2O_3 and MnO_2.

According to the reported literature [27-30] in perovskite oxide systems containing Mn, peaks of MnO exist at 641.0 eV and 652.7 eV with the charge state of +2; the peaks of Mn_2O_3 are located at 641.4 eV and 653.1eV with the charge state of +3; and the peaks of MnO_2 are located at 642.1 eV and 653.8 eV with the charge state of +4.

In order to determine the charge states with respect to the binding energy (BE), each main peak was also deconvoluted, as shown in Fig. 6; peak data is also summarized in Table 3. Comparing the XPS Mn peaks of LSTM powder after heat treatment under oxidizing atmosphere (the LSTM-(1) sample from Table 1) to the peaks of a sample after a heating treatment under reducing atmosphere (the LSTM-(2) sample from Table 1) in Table 3, the BE of the peaks related to MnO and MnO_2 are similar. However, the BEs of $2p_{3/2}$ and $2p_{1/2}$ caused by the existence of MnO_2 are shifted to a relatively higher BE range in the reduced sample LSTM-(2) compared to the oxidized sample LSTM-(1).

In Table 3, it can also be seen that the BE ranges of $2p_{3/2}$ and $2p_{1/2}$, related to MnO and Mn_2O_3 from LSTM impregnated onto a NiO / 8YSZ substrate (the LSTM-(3) sample from Table 1) and partially Ni-removed Ni / 8YSZ substrate (the LSTM-(4) sample from Table 1), show

similar BE values when compared to the value of LSTM under reducing atmosphere.

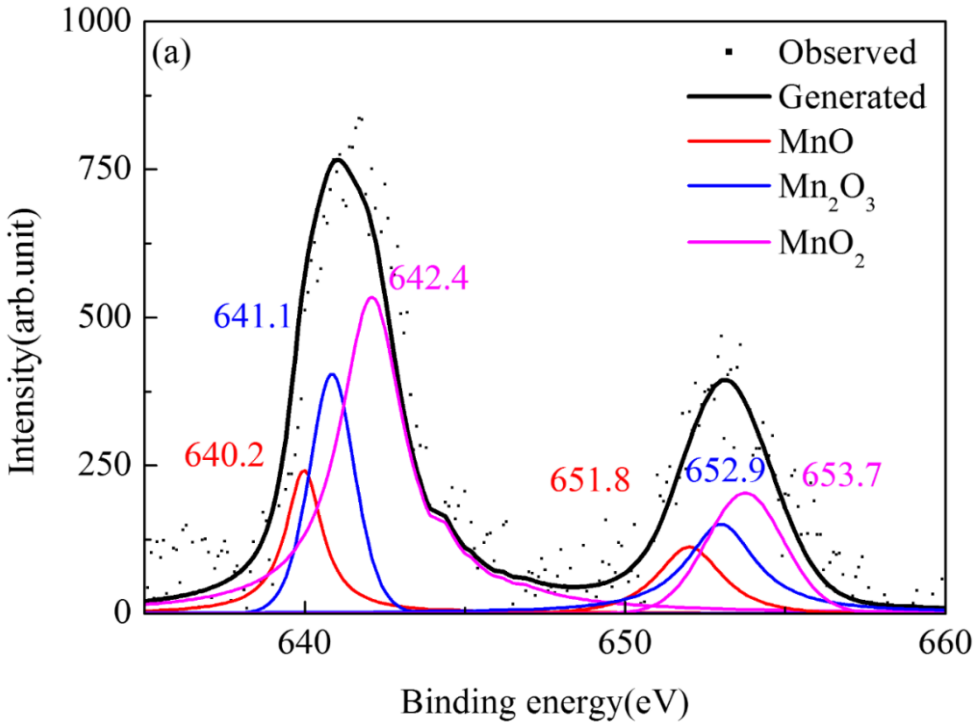

Fig. 6 (a)

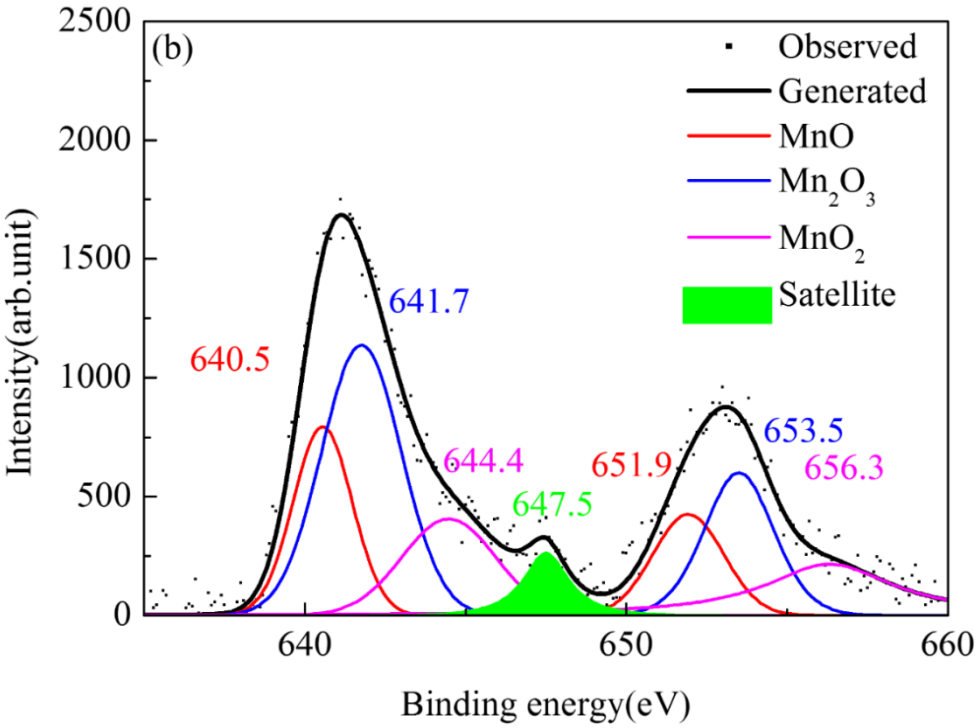

Fig. 6 (b)

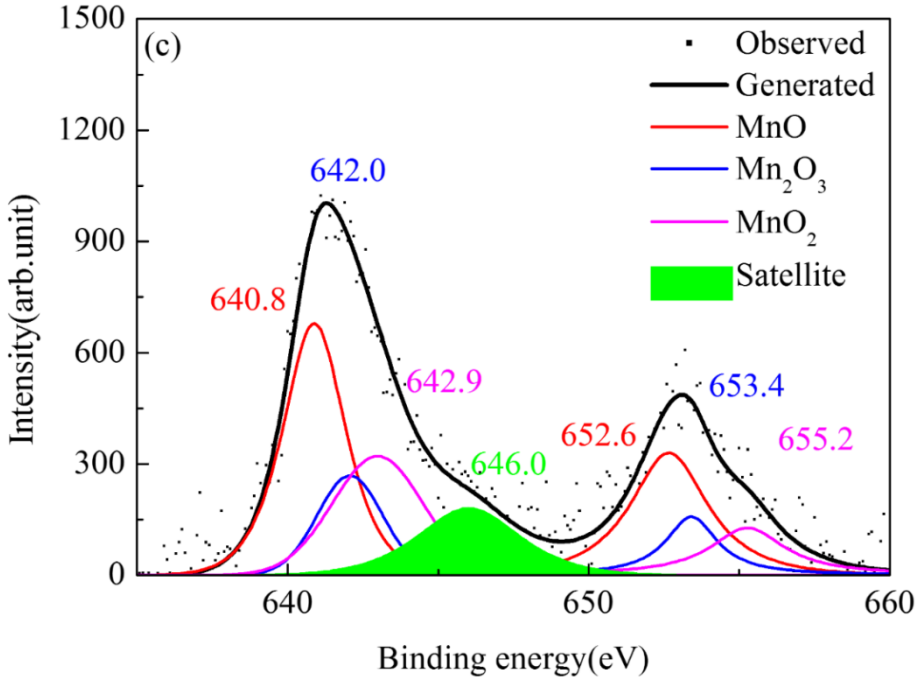

Fig. 6 (c)

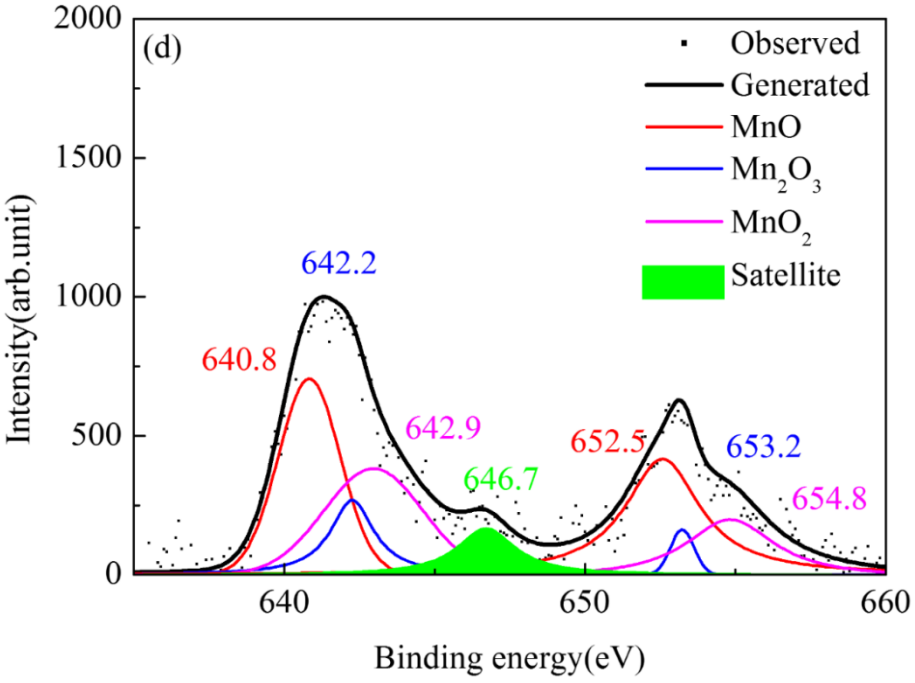

Fig. 6 (d)

Fig. 6 Measured Mn 2p peaks and deconvolution peaks of LSTM (a) LSTM-(1), (b)LSTM-(2), (c) LSTM-(3) and (d) LSTM-(4).

Table 3 also displays the summarized area % of Mn comprising LSTM. From the results shown in Table 3, it can be said that LSTM-(1) contains the highest amount of Mn^{4+} because the area % calculated from $2p_{3/2}$ and $2p_{1/2}$ of MnO_2 was around 54.1 %; therefore, MnO_2 can be seen to exist in a more stable state than MnO and Mn_2O_3. The area %, showing the charge state of Mn^{2+} and Mn^{3+}, contained portions of 17.65 % and 28.25 % of the LSTM-(1) sample.

Most of the charge state of the reduced LSTM (LSTM-(2) sample) was caused by $2p_{3/2}$ and $2p_{1/2}$ of Mn_2O_3, which had a total area % of 47.5; this implies that the main charge state of the reduced LSTM-(2) sample is Mn^{3+}. In the case of LSTM-(3) and LSTM-(4), calculated area % values of 51.12 and 52.65 were found; it can be seen that the most common charge state is Mn^{2+}. In the case of the Mn-O oxide system, the general reduction process of MnO_2 is following a path of reduction leading firstly to Mn_2O_3 and subsequently to MnO ($MnO_2 \rightarrow Mn_2O_3 \rightarrow MnO$); when comparing the reduction processes of the three types MnO_2, Mn_2O_3 and MnO with the highest amount of area % from the LSTM-(1), LSTM-(2), LSTM-(3) and LSTM-(4) samples, these four samples have the same reduction behavior.

The ratios of Mn^{3+} / Mn^{4+} and the charge sate of Mn with the various experimental treatments are also summarized in Table 3. The ratio of Mn^{3+} / Mn^{4+} from LSTM-(1) was calculated and found to be 0.52; the main charge state of Mn with same conditions was found to be 3.36. Interestingly upon calculation of the average charge state of Mn, it was found to be less 3 in all samples exposed to reducing atmosphere. The average charge state of Mn in all samples containing LSTM in contact with a Ni containing substrate, LSTM-(3) and LSTM-(4), is found to be even lower than that of the sample obtained by reducing LSTM-(2), the lowest value observed being 2.78, unsurprisingly in LSTM-(3), the sample with the highest Ni content. The contact with Ni seems to lead to an even deeper state of reduction of Mn in LSTM, in the case

of the LSTM-(3) and (4) samples, the prevalent charge state is Mn^{2+} with ratios of 51.12 % and 52.65 %. In comparison, in the sample reduced without Ni contact, LSTM-(2), the most frequent charge state is Mn^{3+} with a proportional share of 47.50 %.

Significantly, satellite peaks of Mn from fully reduced LSTM-(2), (3) and (4) were observed; these satellite peaks are displayed with green color in Fig. 6 (b), (c) and (d). These satellite peaks apparently are a consequence of reduction, they emerge in all reduced samples, in LSTM-(2), LSTM-(3) and LSTM-(4) they can be found at BEs of 647.5 eV, 646.0 eV and 646. 7 eV respectively, while no evidence of satellite peaks can be observed in the oxidized sample LSTM-(1). Generally, the appearance of satellite peaks is linked to advanced electro-catalytic performance and enhanced electrochemical properties, as reported by M. K. Rath et al. [29]; therefore, reduced LSTM can be used for anode materials of HT-SOFCs.

Table 3. Binding energy (BE) and % area of the Mn 2p peak

	BE peak shift (eV)						**% Area**						**Mn^{3+}/Mn^{4+}**	**Mn Charge**
	MnO (2+)		**Mn_2O_3 (3+)**		**MnO_2 (4+)**		**MnO (2+)**		**Mn_2O_3 (3+)**		**MnO_2 (4+)**			
	$2p_{3/2}$	$2p_{1/2}$	$2p_{3/2}$	$2p_{1/2}$	$2p_{3/2}$	$2p_{1/2}$	$2p_{3/2}$	$2p_{1/2}$	$2p_{3/2}$	$2p_{1/2}$	$2p_{3/2}$	$2p_{1/2}$		
LSTM-(1)	640.2	651.8	641.1	652.9	642.4	653.7	10.65	7.0	16.0	12.25	40.68	13.42	0.52	3.36
LSTM-(2)	640.5	651.9	641.7	653.5	644.4	656.3	16.63	10.71	32.32	15.18	13.51	11.65	1.89	2.98
LSTM-(3)	640.8	652.6	642.0	653.4	642.9	655.2	30.81	20.31	11.93	7.95	19.75	9.25	0.69	2.78
LSTM-(4)	640.8	652.5	642.2	653.2	642.9	654.8	26.61	26.04	10.17	2.33	22.97	11.88	0.36	2.82

3.6. XPS spectra of Ti

The measured and deconvoluted XPS results of Ti 2p for LSTM are shown in Fig. 7. From these results, it can be seen that the Ti 2p peaks can be separated into Ti $2p_{3/2}$ and Ti $2p_{1/2}$, caused by spin-orbital splitting; both Ti $2p_{3/2}$ and Ti $2p_{1/2}$ can be deconvoluted into 3 spectra. When assuming from the deconvolution results in Fig. 7 and the summarized results in Table 4 that various charge states of Ti are present for types of Ti^{2+}, Ti^{3+} and Ti^{4+}, all of the BEs with respect to the various samples are located in almost the same BE ranges; this agrees with our previous experiment on Ti containing complex perovskites [21], as well as with the literature [24, 26, 27]. For example, the XPS peak of TiO_2 forms a charge of Ti^{2+} at BEs of 455.5 eV (Ti $2p_{3/2}$) and 461.1 eV (Ti $2p_{1/2}$) and the XPS peak of Ti_2O_3 forms a charge of Ti^{3+} at 457.3 eV (Ti $2p_{3/2}$) and 462.5 eV (Ti $2p_{1/2}$). In addition, the evidence for the presence of Ti^{4+} of the oxide type of TiO_2 was observed at 458.7 eV (Ti $2p_{3/2}$) and 464.3 eV (Ti $2p_{1/2}$) [21, 29, 31, 32].

Unlike the various BEs that can be seen in the spectra of Mn, the BEs of Ti^{2+}, Ti^{3+} and Ti^{4+}, with respect to the four types of samples, are present in almost the same energy band range. The various charge states of Ti comprising LSTM can be related to the area% of the deconvoluted results; these results are also summarized in Table 4. In the case of the sample annealed in an oxidizing atmosphere, LSTM-(1), the largest portion is occupied by Ti^{4+} with a total area share of 49.9 %. The area % of Ti^{3+} in the LSTM-(1) sample is 41.9 % and that of Ti^{2+} is about 8.19 %. Therefore, it can be seen that the charge state Ti^{4+} is prevalent amongst the Ti species in LSTM-(1). However, deconvolution results of reduced LSTM, expressed as LSTM-(2) sample, show a top value of 45.9% at a BE range ascribed to Ti_2O_3; the main charge of Ti from reduced LSTM, therefore, is Ti^{3+}. When comparing LSTM-(1) with LSTM-(2), LSTM-(1) is found to contain the highest amount of Ti^{4+}. However, LSTM-(2) contains the highest amount of Ti^{3+}. In the same way LSTM-(3) and (4) samples showed Ti_2O_3 peaks

constituting the highest portions of Ti related peaks, with the area % values of 41.79 and 68.02. In summary, a change of Ti to lower charge valence states by applying reducing conditions to LSTM is observed in this XPS analysis, for example the change of Ti^{4+} to Ti^{3+}. The presence of various charge valences such as Ti^{4+} and Ti^{3+} can promote a path for improved electron transport and provide additional pathways for redox reactions in the LSTM oxide system.

The ratio of Ti^{3+} / Ti^{4+} and the average charge sate of Ti under various experimental treatments are also summarized in Table 4. The ratios of Ti^{3+} / Ti^{4+} from LSTM-(1), LSTM-(2), LSTM-(3) and LSTM-(4) were calculated and found to be 0.84, 1.07, 1.14 and 3.40; the calculated average charge states of Ti can be expressed as 3.42, 3.32, 3.15 and 3.10, which indicates that the ratio of Ti^{3+} / Ti^{4+} of the samples increased and the average charge of Ti in the samples decreased during the reduction process leading to a greater concentration of Ti^{3+} instead of Ti^{4+}.

Significantly, in the case of satellite peaks in the Ti XPS spectra shown as Fig. 7, LSTM-(4) is the only sample showing evidence of a satellite peak, while the also fully reduced samples LSTM-(2) and (3) didn't show any satellite peaks. The satellite peak in LSTM-(4) was observed at a BE value of around 460.5 eV, this BE value is very close to the value (460.6 eV) of Ti metal $2p_{1/2}$ reported by M. K. Rath's group [29]. In other words, the existence of a Ti metal peak on the surface of LSTM was only measured for LSTM-(4); the presence of metallic Ti can improve the electro-catalytic reaction. The much higher electrical conductivity of LSTM impregnated into a Ni (R) / 8YSZ substrate compared to all the other samples, as shown in Fig. 3, can be seen as a result of this fact. Therefore, it can be concluded that the satellite peak in the LSTM-(4) sample was generated by LSTM impregnated on a selectively Ni-removed Ni / 8YSZ (Ni (R) / 8YSZ) substrate under reducing condition.

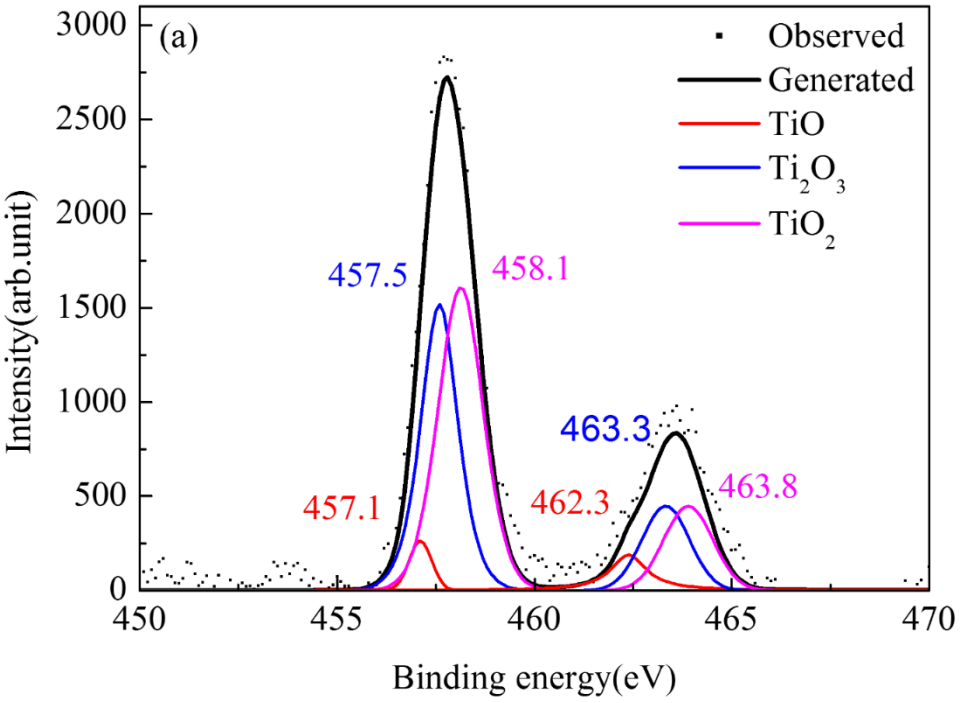
(a)
Observed
Generated
TiO
Ti2O3
TiO2
457.5
458.1
463.3
457.1
462.3
463.8
Intensity(arb.unit)
Binding energy(eV)
3000
2500
2000
1500
1000
500
0
450
455
460
465
470

Fig. 7 (a)

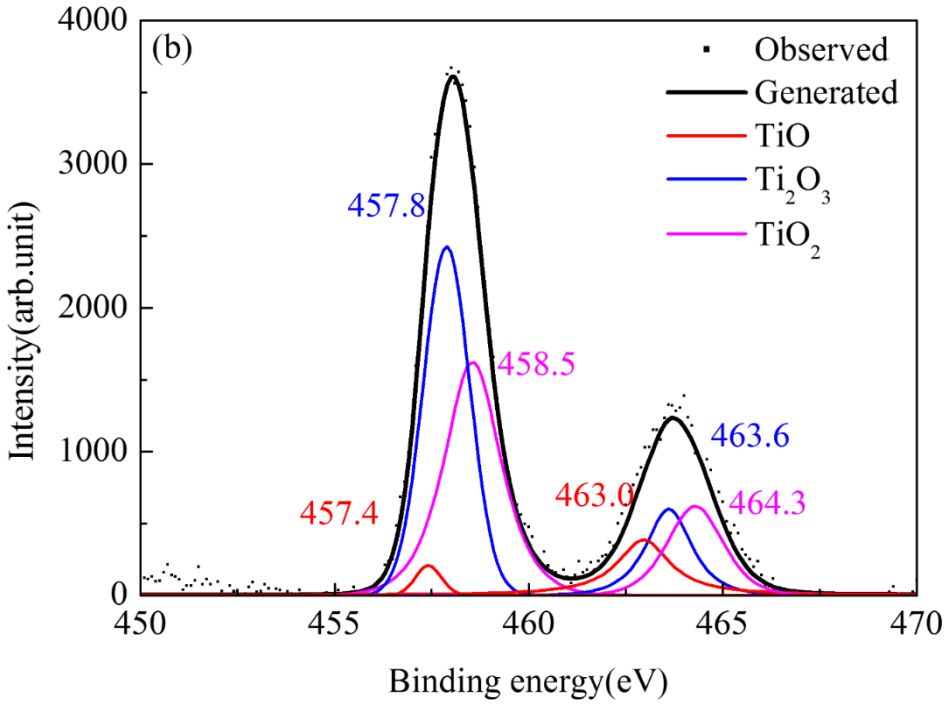
(b)
Observed
Generated
TiO
Ti2O3
TiO2
457.8
458.5
463.6
457.4
463.0
464.3
Intensity(arb.unit)
Binding energy(eV)
4000
3000
2000
1000
0
450
455
460
465
470

Fig. 7 (b)

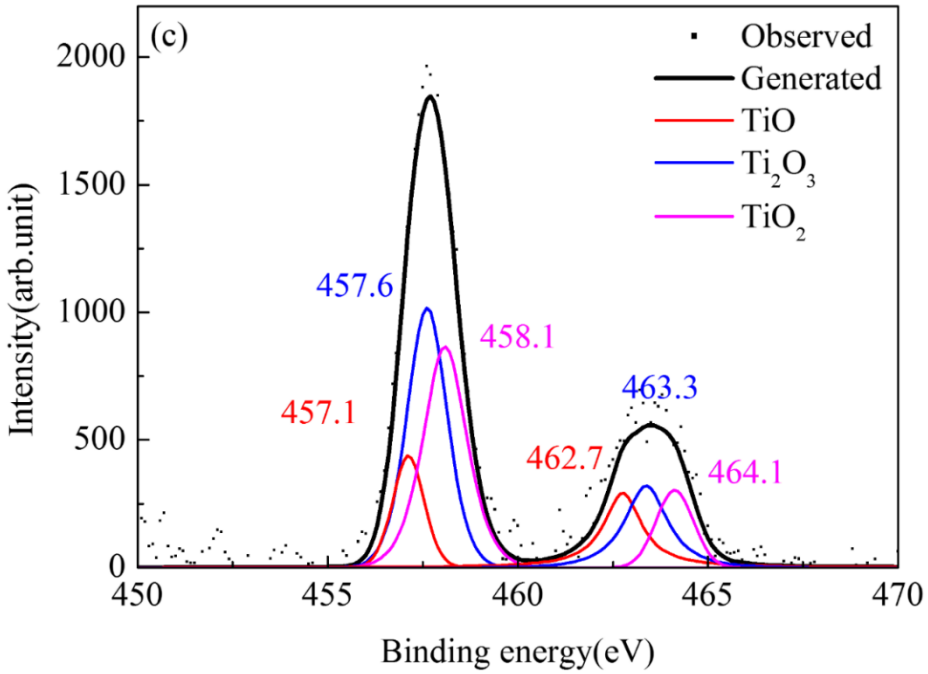

Fig. 7 (c)

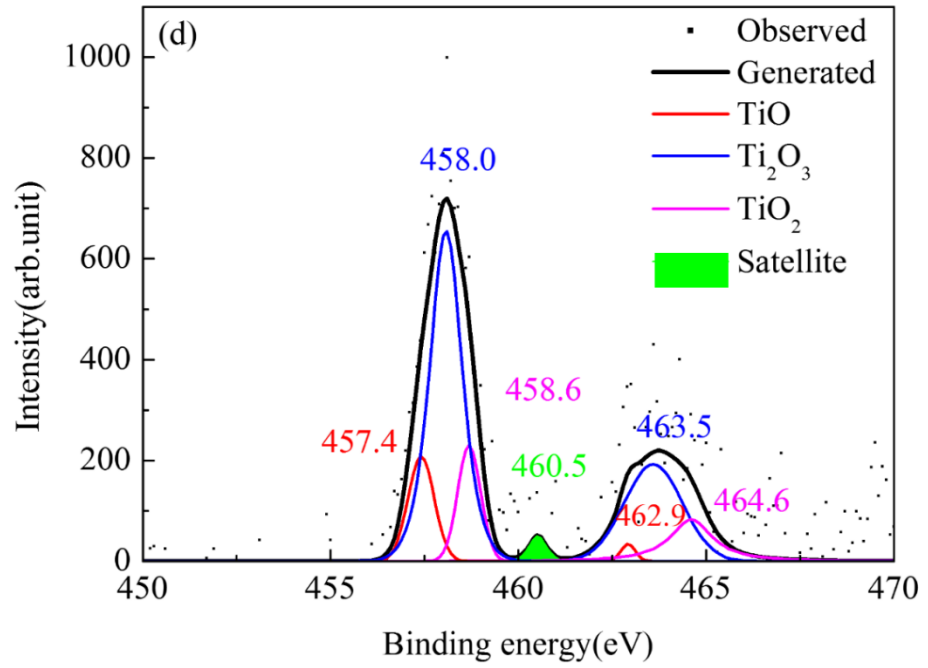

Fig. 7 (d)

Fig. 7 Measured Ti 2p peaks and deconvolution peaks of LSTM (a) LSTM-(1), (b)LSTM-(2), (c) LSTM-(3) and (d) LSTM-(4).

Table 4. Binding energy (BE) and % area of the Ti 2p peaks

	BE peak shift (eV)						**Area %**						**Ti^{3+}/Ti^{4+}**	**Ti Charge**
	TiO (2+)		**Ti_2O_3 (3+)**		**TiO_2 (4+)**		**TiO (2+)**		**Ti_2O_3 (3+)**		**TiO_2 (4+)**			
	$2p_{3/2}$	$2p_{1/2}$	$2p_{3/2}$	$2p_{1/2}$	$2p_{3/2}$	$2p_{1/2}$	$2p_{3/2}$	$2p_{1/2}$	$2p_{3/2}$	$2p_{1/2}$	$2p_{3/2}$	$2p_{1/2}$		
LSTM-(1)	457.1	462.3	457.5	463.3	458.1	463.8	3.09	5.10	30.90	11.0	38.56	11.35	0.84	3.42
LSTM-(2)	457.4	463.0	457.8	463.6	458.5	464.3	1.72	9.21	36.14	9.80	31.52	11.61	1.07	3.32
LSTM-(3)	457.1	462.7	457.6	463.3	458.1	464.1	10.02	11.42	30.09	11.70	28.61	8.16	1.14	3.15
LSTM-(4)	457.4	462.9	458.0	463.5	458.6	464.6	10.99	0.98	45.48	22.54	10.65	9.36	3.40	3.10

4. Conclusions

The electrical conductivity values of LSTM impregnated onto a Ni (R) / 8YSZ were surprisingly much higher than those of a pure Ni (E) / 8YSZ substrate.

When comparing the BE values of $2p_{3/2}$ and $2p_{1/2}$ from LSTM under oxidizing and reducing atmosphere conditions, the values under reducing atmosphere condition can be seen to have shifted to higher BE ranges. LSTM-(1) had the highest amount of Mn^{4+} at 54.10 %. However, LSTM-(2) exposed to reducing condition showed the highest amount of Mn^{3+} because Mn^{4+} is reduced to Mn^{3+}. The charge state of Mn from the LSTM impregnated samples, such as LSTM-(3) and LSTM-(4) in the reducing atmosphere, showed a lower change depending on the support from Mn^{3+} to Mn^{2+}. Significantly, satellite peaks of Mn were found only in the reducing atmosphere condition, which indicates that the reduced samples (LSTM-(2), (3) and (4)) may have advanced electro-catalytic properties. In the case of the charge state of Ti, most of the Ti^{4+} was present in the LSTM exposed to the oxidizing atmosphere condition. The reduction of the charge state in Ti showed the same tendency as that of Mn. Unlike the satellite peaks of Mn, however, among the four samples, the only satellite peak of Ti known as the presence of metal Ti was found in the LSTM- (4) sample.

Acknowledgements

This research was supported by Basic Science Research Program through the National Research Foundation of Korea (NRF) funded by the Ministry of Science, ICT & Future Planning (No. 2014R1A1A1004163) and by the Korea Institute of Energy Technology Evaluation and Planning (KETEP) and the Ministry of Trade, Industry & Energy (MOTIE) of the Republic of Korea (No. 20184030201900 and No. 20182010600400).

References

[1] H. Kishimoto, K. Yamaji, T. Horita, Y. Xiong, N. Sakai N, M. E. Brito, H. Yokokawa, Feasibility of liquid hydrocarbon fuels for SOFC with Ni-ScSZ anode, J. Power Sources 172 (2007) 67-71.

[2] S.P. Yoon, J. Han, S.W. Nam, T.-H. Lim, S.-A. Hong, Improvement of anode performance by surface modification for solid oxide fuel cell running on hydrocarbon fuel, J. Power Sources 136 (2004) 30-36.

[3] A Ringuedé, J.A Labrincha, J.R Frade, A combustion synthesis method to obtain alternative cermet materials for SOFC anodes, Solid State Ionics 141-142 (2001) 549-557.

[4] W.Z. Zhu, S.C. Deevi, A review on the status of anode materials for solid oxide fuel cells, Mater. Sci. Eng., A 362 (2003) 228-239.

[5] T. Takeguchi, R. Kikuchi, T. Yano, K. Eguchi, K. Murata, Effect of precious metal addition to Ni-YSZ cermet on reforming of CH_4 and electrochemical activity as SOFC anode, Catal. Today 84 (2003) 217-222.

[6] Z. Zhan, S.A. Barnett, Use of a catalyst layer for propane partial oxidation in solid oxide fuel cells, Solid State Ionics 176 (2005) 871-879.

[7] C. Lu, W.L Worrell, C Wang, S Park, H Kim, J.M. Vohs, R.J. Gorte, Development of solid oxide fuel cells for the direct oxidation of hydrocarbon fuels, Solid State Ionics 152-153 (2002) 393-397.

[8] S. An, C. Lu, W.L. Worrell, R.J. Gorte, J.M. Vohs, Characterization of Cu-CeO_2 direct hydrocarbon anodes in a solid oxide fuel cell with lanthanum gallate electrolyte, Solid State Ionics 175 (2004) 135-138.

[9] J. Sfeir, $LaCrO_3$-based anodes: stability considerations, J. Power Sources 118 (2003) 276-285.

[10] S.P. Jiang, X. J. Chen, S.H. Chan, J.T. Kwok, K.A. Khor, $(La_{0.75}Sr_{0.25})(Cr_{0.5}Mn_{0.5})O_3$/YSZ composite anodes for methane oxidation reaction in solid oxide fuel cells, Solid State Ionics 177 (2006) 149-157.

[11] Y. Kim, J. H. Kim, J. Bae, C. W. Yoon, S. W. Nam, In situ analyses of carbon dissolution into Ni-YSZ anode materials, J. Phys. Chem. C 116 (2012) 13281-13288.

[12] J. B. Goodenough, H. Yun-Hui, Alternative anode materials for solid oxide fuel cells, J. Power Sources 173 (2007) 1-10.

[13] W. A. Rosensteel, S. M.Babiniec, D. D.Storjohann, J. Persky, N. P. Sullivan, Use of anode barrier layers in tubular solid-oxide fuel cells for robust operation on hydrocarbon fuels, J. Power Sources 205 (2012) 108-13.

[14] J. C. Ruiz-Morales, J. Canales-Vázquez, C. Savaniu, D. Marrero-López, W. Zhou, J. T. S. Irvine, Disruption of extended defects in solid oxide fuel cell anodes for methane oxidation, Nature 439 (2006) 568-571.

[15] J. C. Ruiz-Morales, J. Canales-Vázquez, C. Savaniu, D. Marrero-López, P. Núñez, W. Zhou, J. T. S. Irvine, A new anode for solid oxide fuel cells with enhanced OCV under methane operation, Phys. Chem. Chem .Phys. 9 (2007) 1821-1830.

[16] Z. Cao, L. Fan, G. Zhang, K. Shao, C. He, Q. Zhang, Z. Lv, B. Zhu, Titanium-substituted ferrite perovskite: An excellent sulfur and coking tolerant anode catalyst for SOFCs, Catal. Today 330 (2019) 217-221.

[17] J. H. Kim, D. Miller, H. Schlegl, D. McGrouther, J. T. S. Irvine, Investigation of microstructural and electrochemical properties of impregnated (La,Sr)(Ti,Mn)$O_{3\pm\delta}$ as a potential anode material in high-temperature solid oxide fuel cells, Chem. Mater. 23 (2011) 3841-3847.

[18] J. H. Kim, H. Schlegl, J. T. S. Irvine, The catalytic effect of impregnated (La, Sr)(Ti,

Mn)$O_{3\pm d}$ with CeO_2 and Pd as potential anode materials in high temperature solid oxide fuel cells, Int. J. Hydrogen Energy 37 (2012) 14511-14517.

[19] M. Asamoto, M. Hino, S. Yamaguchi, H. Yahiro, Transformation of crystalline heteronuclear cyano complex to crystalline perovskite-type oxide by thermal decomposition, Catal. Today 175 (2011) 534-540.

[20] D. Lee, I. Lee, Y. Jeon, R. Song, Characterization of scandia stabilized zirconia prepared by glycine nitrate process and its performance as the electrolyte for IT-SOFC, Solid state Ionics, 176 (2005) 1021-1025.

[21] K. Kim, J. Jeong, A. K. Azad, S. B. Jin, J. H. Kim, X-ray photoelectron spectroscopic study of direct reforming catalysts $Ln_{0.5}Sr_{0.5}Ti_{0.5}Mn_{0.5}O_{3\pm d}$ (Ln = La, Nd, and Sm) for high temperature-operating solid oxide fuel cell, Appl. Surf. Sci. 365 (2016) 38-46.

[22] Y.-H. Joung, H. I. Kang, W. S. Choi, J. H. Kim, Investigation of x-ray photoelectron spectroscopy and electrical conductivity properties of the layered perovskite $LnBaCo_2O_{5+d}$ (Ln = Pr, Nd, Sm, and Gd) for IT-SOFC, Electron. Mater. Lett. 9 (2013) 463-465.

[23] J. H. Kim, X-ray photoelectron spectroscopy analysis of $(Ln_{1-x}Sr_x)CoO_{3-\delta}$ (Ln: Pr, Nd and Sm), Appl. Surf. Sci. 258 (2011) 350-355.

[24] Y. Kim, H. Schlegl, K. Kim, J. T.S. Irvine, J. H. Kim, X-ray photoelectron spectroscopy of Sm-doped layered perovskite for intermediate temperature-operating solid oxide fuel cell, Appl. Surf. Sci. 288 (2014) 695-701.

[25] J. F. Moulder, W. F. Stickle, P. E. Sobol, K. D. Bomben, Handbook of x-ray photoelectron spectroscopy: a reference book of standard spectra for identification & interpretation of XPS data, Perkin-Elmer Corp, Eden Prairie, MN, 1992.

[26] M. Ghaffari, Surface state and band structure studies of $SrTi_{(1-x)}Fe_{(x)}O_{(3-d)}$ (x=0-1) perovskite-type nano structure by x-ray and ultraviolet photoelectron spectroscopy, Surf.

Sci. 606 (2012) 670-677.

[27] X. Fu, F. Tietz, D. Stöver, $La_{0.4}Sr_{0.6}Ti_{1-x}Mn_xO_{3-\delta}$ perovskites as anode materials for solid oxide fuel cells electrochemical synthesis and engineering, J. Electrochem. Soc. 153 (2006) D74-D83.

[28] S. Tao, J.T.S. Irvine, A redox-stable efficient anode for solid-oxide fuel cells, Nat. Mater. 2 (2003) 320-323.

[29] M.K. Rath, Effects of manganese substitution at the B-site of lanthanum-rich strontium titanate anodes on fuel cell performance and catalytic activity, Ceram. Int. 39 (2013) 6343-6353.

[30] S. Tao, J.T.S. Irvine, Synthesis and characterization of $(La_{0.75}Sr_{0.25})Cr_{0.5}Mn_{0.5}O_{3-\delta}$, a redox-stable, efficient perovskite anode for SOFCs, J. Electrochem. Soc. 151 (2004) A252-A259.

[31] V. R. Mastelaro, P. N. Lisboa-Filho, P. P. Neves, W. H. Schreiner, P. A.P. Nascente, J. A. Eiras, X-ray photoelectron spectroscopy study on sintered $Pb_{1-x}La_xTiO_3$ ferroelectric ceramics, J. Electron. Spectrosc. Relat. Phenom. 156-158 (2007) 476-481.

[32] M. Viviani, M.T. Buscaglia, P. Nanni, R. Parodi, G. Gemme, A. Dacca , XPS investigation of surface properties of $Ba_{(1-x)}Sr_xTiO_3$ powders prepared by low temperature aqueous synthesis, J. Eur. Ceram. Soc. 19 (1999) 1047-1051.

Conflict of Interest

Title: "X-ray photoelectron spectroscopic study of impregnated $La_{0.4}Sr_{0.6}Ti_{0.8}Mn_{0.2}O_{3\pm d}$ anode material for high temperature-operating solid oxide fuel cell"

We authors confirm that this manuscript has not been published elsewhere and is not under consideration by another journal. All authors have approved the final modified manuscript and agreed with resubmission to Solid State Ionics. We have read and have abided by the statement of ethical standards for manuscript to Solid State Ionics. We authors have no conflicts of interest to declare.

Sung Hun Woo, Department of Advanced Materials Science and Engineering, Hanbat National University

Dae Soo Park, Department of Advanced Materials Science and Engineering, Hanbat National University

WonSeok Choi, Department of Electrical Engineering, Hanbat National University

Hyunil Kang, Department of Electrical Engineering, Hanbat National University

Seung-Wook Baek, Division of Industrial Metrology, Korea Research Institute of Standards and Science (KRISS)

Hyun-Suk Kim, Department of Materials Science and Engineering, Chungnam National University

Tae Ho Shin, Energy and Environment Division, Korea Institute of Ceramic Engineering and Technology (KICET)

Jun-Young Park, Department of Nanotechnology and Advanced Materials Engineering, Sejong University

Harald Schlegl, Engineering Department, Lancaster University

Jung Hyun Kim, Department of Advanced Materials Science and Engineering, Hanbat National University

Author Statement

Title: "X-ray photoelectron spectroscopic study of impregnated $La_{0.4}Sr_{0.6}Ti_{0.8}Mn_{0.2}O_{3\pm d}$ anode material for high temperature-operating solid oxide fuel cell"

Sung Hun Woo carried out the experiment and wrote the manuscript with support from **Jung Hyun Kim**.

Dae Soo Park carried out the experiment and wrote the manuscript with support from **Jung Hyun Kim**.

WonSeok Choi analyzed XPS spectra and contributed to the interpretation of the results.

Hyunil Kang analyzed XPS spectra and contributed to the interpretation of the results.

Seung-Wook Baek performed the impregnation experiments and contributed to sample preparation.

Hyun-Suk Kim performed the impregnation experiments and contributed to sample preparation.

Tae Ho Shin provided critical feedback and helped shape the research, analysis and manuscript.

Jun-Young Park performed the electrical conductivity measurements for the suggested experiment.

Harald Schlegl helped shape the research, analysis and manuscript. He also conducted the English spelling, grammar and proofreading and wrote the manuscript with **Jung Hyun Kim**.

Jung Hyun Kim planned the experiments, supervised the work, analyzed research results and took the lead in writing the manuscript.